



Provided by the author(s) and University of Galway in accordance with publisher policies. Please cite the published version when available.

Title	A dislocation mechanics constitutive model for effects of welding-induced microstructural transformation on cyclic plasticity and low-cycle fatigue for X100Q bainitic steel
Author(s)	Devaney, Ronan J.; Barrett, Richard A.; O'Donoghue, Padraic E.; Leen, Sean B.
Publication Date	2020-12-14
Publication Information	Devaney, Ronan J., Barrett, Richard A., O'Donoghue, Padraic E., & Leen, Seán B. (2021). A dislocation mechanics constitutive model for effects of welding-induced microstructural transformation on cyclic plasticity and low-cycle fatigue for X100Q bainitic steel. <i>International Journal of Fatigue</i> , 145, doi: https://doi.org/10.1016/j.ijfatigue.2020.106097
Publisher	Elsevier
Link to publisher's version	https://doi.org/10.1016/j.ijfatigue.2020.106097
Item record	http://hdl.handle.net/10379/16669
DOI	http://dx.doi.org/10.1016/j.ijfatigue.2020.106097

Downloaded 2024-04-17T22:08:22Z

Some rights reserved. For more information, please see the item record link above.





A dislocation mechanics constitutive model for effects of welding-induced microstructural transformation on cyclic plasticity and low-cycle fatigue for X100Q bainitic steel

Ronan J. Devaney^{a,c}, Richard A. Barrett^{a,c}, Padraic E. O'Donoghue^{b,c}, Seán B. Leen^{a,c,*}

^a Mechanical Engineering, School of Engineering, NUI Galway, Ireland

^b Civil Engineering, School of Engineering, NUI Galway, Ireland

^c Ryan Institute for Environmental, Marine and Energy Research, NUI Galway, Ireland

ARTICLE INFO

Keywords:

Microstructure
Bainite
Welding
Fatigue
Cyclic plasticity
Heat affected zone

ABSTRACT

This paper presents a physically-based cyclic viscoplasticity model to capture the influence of welding-induced microstructural transformation on the fatigue response of the bainitic high-strength low-alloy steel, X100Q. The model incorporates the strengthening effects of dislocations, microstructural boundaries and precipitates, and the softening effects of microstructural degradation and early-life fatigue damage on yield strength and nonlinear cyclic-plastic response. The model is applied to predict the constitutive responses of X100Q parent material, physically-simulated intercritical heat affected zone (HAZ) and fine-grained HAZ, based on differences in bainitic hierarchical microstructure between the materials. A refined bainitic block structure is shown to be the primary microstructural feature contributing to monotonic and cyclic strength in the materials, whereas dislocation annihilation and the concomitant coarsening of the bainitic lath structure with cyclic-plastic deformation leads to cyclic softening behaviour.

1. Introduction

As offshore oil and gas production moves to deep- and ultra-deepwaters, such as the Shell Stones field at a sea depth of 2,926 m [1], cost-effective riser solutions are required to conduct hydrocarbons and injection fluids between the seabed and production facility. Steel catenary risers (SCRs), manufactured using high-strength low-alloy steels, are suited to this application due to their high-pressure capacity and relatively low costs. However, due to the extreme dynamic loading associated with the offshore environment, fatigue performance is a primary factory for SCR design.

In particular, the discontinuities and defects associated with welded connections, such as misalignment, lack of fusion, and welding-induced microstructural transformations cause stress concentrations which may result in localised plasticity and fatigue hot-spots ([2–4]). Due to the high thermal gradients which occur during welding in the parent material (PM) adjacent to the joint, a graded inhomogeneous heat affected zone (HAZ) microstructure is formed [5]. The constitutive and fatigue performance of the material within the HAZ may deviate significantly from that of the PM [4]. Therefore, an accurate representation of the

variation in mechanical response across the HAZ is required to model the constitutive response of welded connections, and therefore determine fatigue performance at these hot-spot locations.

A common approach to this issue is demarcation of the HAZ into regions of assumed homogeneous response for modelling. For example, Farragher and co-workers [6] addressed this issue by deriving a bulk response for the HAZ from PM, cross-weld and weld metal (WM) fatigue test data. Touboul et al. [7] used digital image correlation to extract the tensile response of PM, intercritical HAZ (ICHAZ), fine-grained HAZ (FGHAZ) and WM from cross-weld tensile tests. However, this methodology typically assumes variation of mechanical properties in only one direction and is likely to omit local maxima or minima in mechanical performance and introduce artificial discontinuities unless the HAZ is demarcated into several regions.

Physically-based modelling is another approach to this problem, where the mechanical response of the material is predicted based on known physical constants and measurable microstructural characteristics. This methodology is particularly suited to modelling the HAZ when used in conjunction with full-field microstructural measurements or a microstructure evolution model. The methodology is predicated on the

* Corresponding author.

E-mail address: sean.leen@nuigalway.ie (S.B. Leen).

<https://doi.org/10.1016/j.ijfatigue.2020.106097>

Received 9 October 2020; Received in revised form 6 December 2020; Accepted 7 December 2020

Available online 14 December 2020

0142-1123/© 2020 The Authors. Published by Elsevier Ltd. This is an open access article under the CC BY license (<http://creativecommons.org/licenses/by/4.0/>).

mechanism of plastic deformation via dislocation glide, first described by Volterra [8]. Building on this theory, Bergström and Roberts ([9,10]) and Mecking and Kocks ([11,12]) developed dislocation mechanics models to capture the effect of dislocation density evolution on constitutive response using a material average basis. However, this methodology is not suitable for application to materials with hierarchical microstructures, such as bainite or martensite, due to the influence of microstructural boundaries on the dislocation evolution processes.

To address this issue, He et al. [13] modified the Kocks-Mecking model to account for the effect of bainitic lath width and the inhomogeneous distribution of dislocations across lath boundaries and interiors. Estrin et al. [14] implemented a volume fraction approach to model the inhomogeneous dislocation density evolution across microstructural cell walls and cell interiors. Roters and co-workers [15] implemented a similar methodology, including probability-based methods to model dislocation density evolution. This methodology was extended to model the hierarchical martensitic microstructure of 9Cr powerplant steels by Magnusson and Sandström [16]. Barrett et al. [17] developed a dislocation-mechanics based cyclic viscoplastic modelling framework, based on a modified hyperbolic sine flow rule, which encompassed dislocation evolution based on the work of Roters et al. [15] and Hosseini et al. [18]. The framework includes the strengthening effects of inhomogeneous precipitate distribution, high-angle boundaries (HABs) and low-angle boundaries (LABs), and the softening effect of lath coarsening via dislocation annihilation. In following work, Barrett et al. [19] developed a physically-based yield strength model, which included the effect of Peierls stress, LABs, HABs, precipitates and solid solutions on yield stress.

In this work, a physically-based cyclic viscoplasticity model based on dislocation mechanics is implemented to capture the influence of inhomogeneous microstructure and microstructure evolution on the cyclic response of PM and HAZ for the bainitic line pipe steel, X100Q. The model is applied here to bainite for the first time and incorporates the strengthening effects of HABs, LABs, dislocation density and precipitates, and the cyclic softening effects of dislocation annihilation, LAB coarsening and early-life fatigue damage. The model is implemented within an implicit MATLAB viscoplasticity programme and used to predict the distinct constitutive responses of (i) X100Q PM, (ii) simulated ICHAZ and (iii) simulated FGHAZ [4] based on measured microstructural characteristics and precipitate volume fractions and dimensions obtained from MatCalc simulations. Finally, the predicted evolutions of dislocation density, lath width and yield strength for X100Q PM, simulated FGHAZ and simulated ICHAZ are compared.

2. Methodology

2.1. Model framework

The physically-based modelling methodology is based on the dislocation-mechanics framework described by Barrett et al. [17] for 9Cr steels but is adapted here to predict the constitutive behaviour of bainitic X100Q steel. The framework is predicated on the evolution of microstructure during cyclic loading, such that the inelastic strain rate is defined as:

$$\dot{\epsilon}^{\text{in}} = f(d_g, w, \lambda, \rho) \quad (1)$$

where d_g is block size, which is the smallest HAB structure within the bainitic microstructure, w is bainitic lath width, λ is precipitate spacing and ρ is dislocation density. For cyclic deformation, the inelastic strain rate is defined using a hyperbolic sine formulation based on Helmholtz free energy, ΔF , and activation volume, ΔV , as follows [17]:

$$\dot{\epsilon}^{\text{in}} = A \exp\left(\frac{-\Delta F}{k_B T}\right) \sinh\left(\frac{\sigma_v \Delta V}{M k_B T}\right) \text{sgn}(\sigma - \sigma_b) \quad (2)$$

where A is the pre-exponential viscous constant, k_B is Boltzmann's

constant, M is the Taylor factor (2.73 [20]), σ_v is viscous stress, σ is stress, σ_b is the kinematic back-stress. The effect of temperature, T (assumed here as 293 K), is included through the use of Arrhenius-type terms in Eq. (2). The viscous stress is defined as follows for uniaxial loading:

$$\sigma_v = |\sigma - \sigma_b| - \sigma_y^{\text{cyc}} \quad (3)$$

where σ_y^{cyc} is the isotropic yield strength. A flowchart illustrating the model inputs and the non-linear iterative solving processes used in the implementation of the physically-based constitutive model in a uniaxial MATLAB code is shown in Fig. 1.

2.2. Kinematic hardening

The kinematic back-stress occurs due to the retardation of dislocation motion or the immobilisation of dislocations at obstacles within the bainitic microstructure, namely: (i) HABs, (ii) LABs and (iii) precipitates [21]. Therefore, the kinematic back-stress is modelled using partial back stresses to account for the influence of these mechanisms as follows:

$$\sigma_b = \sigma_g + \sigma_w + \sigma_p \quad (4)$$

where σ_g is the back-stress due to HABs, σ_w is the back-stress due to LABs and σ_p is the back-stress due to precipitates. The HAB back-stress occurs due to the accumulation of dislocations in pile-ups at HABs [22] and the resultant local stress field. Derived from the model of Ashby et al. [23], the evolution of kinematic back-stress with dislocation pile-ups is [17]:

$$\dot{\sigma}_g = \frac{M b \mu}{\alpha_g} \left(\frac{d_g n_g}{d_g^2} \right) \quad (5)$$

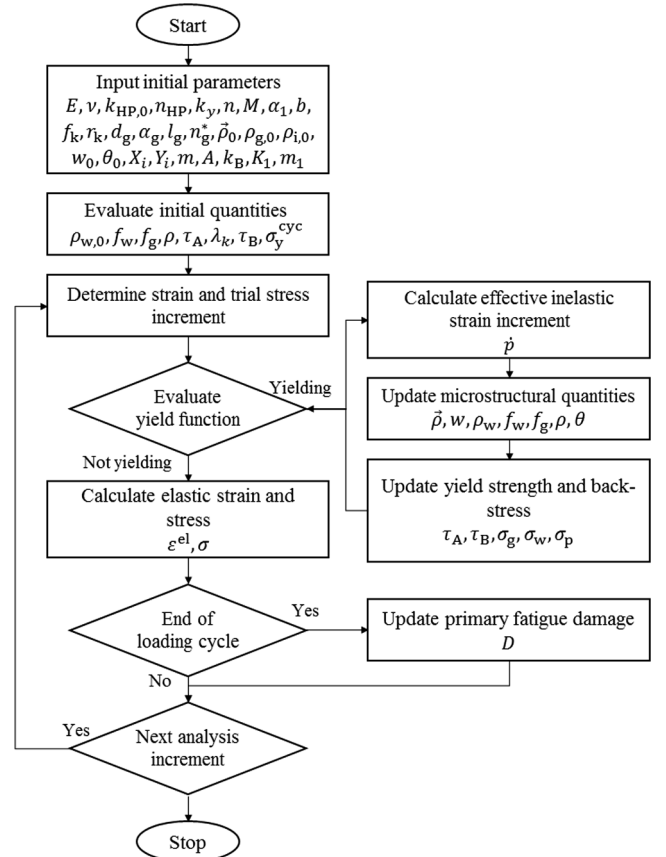


Fig. 1. Flowchart illustrating the implementation of the physically-based constitutive model in an implicit uniaxial MATLAB code.

where b is the magnitude of the Burger's vector (0.248 nm [24]), μ is the shear modulus, α_g is the HAB hardening constant (taken as 0.85) and n_g is the number of dislocations in the pile-up. The bainitic block size, d_g , is used to represent the mean distance between HABs. The dislocation pile-up evolution is formulated by accounting for the probability of interactions between dislocations of opposite sign, as described by Sinclair and co-workers [25], and is given for cyclic deformation by Bardel et al. [26] as:

$$\dot{n}_g = \frac{Ml_g}{b} \left(1 - \frac{n_g}{n_g^* \text{sgn}(\dot{\epsilon}^{\text{in}})} \right) \dot{\epsilon}^{\text{in}} \quad (6)$$

where l_g is the mean spacing between slip lines (taken as 300 nm [17]), n_g^* is the number of sites available for a dislocation to contribute to the dislocation pile-up (taken as 15.6 [17]) and l_g/b is the number of dislocations required to generate deformation.

The back-stress generated due to the presence of LABs is a result of the tendency for dislocations to remain in the stable dislocation cell network formed by bainitic laths, as described by Keller [27]. The evolution of LAB back-stress is derived from the model of Li as ([28,29]):

$$\dot{\sigma}_w = \frac{M\mu}{1-\nu} \left(\frac{0.45bw}{2\pi\theta} \right)^{1/2} \left(\frac{w\dot{\theta} - \theta\dot{w}}{w^2} \right) \quad (7)$$

where ν is Poisson's ratio, which is taken as 0.3. and θ is lath misorientation angle.

The two primary precipitate types which are present in X100Q are M_7C_3 carbides ($M = \text{Mn, Fe, Cr, Mo}$) and MX carbonitrides ($M = \text{Nb, Mo, C; X = C, N}$). The larger M_7C_3 carbides nucleate at HABs, whereas the smaller MX carbonitrides are uniformly distributed throughout the microstructure. This inhomogeneous precipitate distribution can be seen in the transmission electron microscopy (TEM) micrographs obtained by Wang and co-workers [30], for X100Q quenched from peak temperatures in the range of 875 °C to 975 °C, shown in Fig. 2.

The precipitate radii and volume fractions for X100Q PM and simulated HAZ microstructures are assumed to be equal in this work. The equilibrium values were predicted using a MatCalc simulation and are shown in Table 1.

The predicted total volume fraction of precipitates is close to the range of 3–3.6% reported by Wang and co-workers [30] for X100Q. Precipitates contribute to the kinematic back-stress through an Orowan looping process whereby the dislocation loops create a local stress field which impedes subsequent dislocation motion. This phenomenon has been experimentally observed for X80 [31] pipeline steel. As both M_7C_3 and MX precipitates contribute to this back-stress, a rule of mixtures approach ([16,17,14]) is used to account for the inhomogeneous precipitate distributions at boundaries and lath interiors, such that the kinematic back-stress is:

Table 1

The radius and volume fraction of precipitates in X100Q.

Precipitate	Radius (nm)	Volume fraction (%)	Source
M_7C_3	25	2	Present work
MX	10	0.05	Present work

$$\sigma_p = (f_w + f_g)\sigma_{p,\text{BND}} + (1 - f_w - f_g)\sigma_{p,\text{INT}} \quad (8)$$

where f_w and f_g are the volume fractions of the LAB and HAB regions, respectively, and $\sigma_{p,\text{BND}}$ and $\sigma_{p,\text{INT}}$ are the precipitate-induced kinematic back-stress components at boundaries and lath interiors, respectively. A modified version of the Fisher-Hart-Pry [32] model, derived by Barrett et al. [17] for cyclic deformation, is used to calculate the evolution of precipitate-induced back-stresses:

$$\dot{\sigma}_{p,j} = \left[1.24M \left(\frac{\sigma_{\text{Or},j} \mu K}{n} \right)^{1/2} \frac{f_{j,\text{eq}}^{3/4}}{\sqrt{\rho_{\text{cyc}}}} + 3.09 \frac{M^2 \mu K}{n} f_{j,\text{eq}}^{3/2} \right] \dot{p} \text{sgn}(\sigma - \sigma_b) \quad (9)$$

where $\sigma_{\text{Or},j}$ are Orowan stresses, $f_{j,\text{eq}}$ are equivalent volume fractions (where $j = \text{BND, INT}$ representing the boundary and interior regions, respectively), n is the number of active slip systems (taken as 5 [33]), \dot{p} is the accumulated effective inelastic strain rate and ρ_{cyc} is the effective inelastic strain accumulated during a load reversal. The constant, K , is defined as [32]:

$$K = 1 + \frac{1}{2} \left(\frac{\nu}{1-\nu} \right) \quad (10)$$

and the Orowan stress is defined as:

$$\sigma_{\text{Or},j} = M\phi \frac{\mu b}{\lambda_j} \quad (11)$$

where ϕ is the obstacle strength coefficient (taken as 0.7 [34]), and λ_j is the mean obstacle spacing. Due to the inhomogeneous distribution of M_7C_3 carbides, the mean obstacle spacing at the boundaries and within lath interiors is defined as:

$$\lambda_{\text{BND}} = \sqrt{\frac{\lambda_c^2 \lambda_m^2}{\lambda_c^2 + \lambda_m^2}} \quad (12)$$

$$\lambda_{\text{INT}} = \lambda_m \quad (13)$$

where λ_m and λ_c are the mean inter-particle spacings of the MX carbonitrides and M_7C_3 carbides, respectively. The mean inter-particle spacing is defined by accounting for the distance between a critical pair of precipitates for dislocation pinning [35] with the factor 1.2 and the conversion from mean square planar to volumetric radius by using the factor $\sqrt{3/2}$, as [15]:

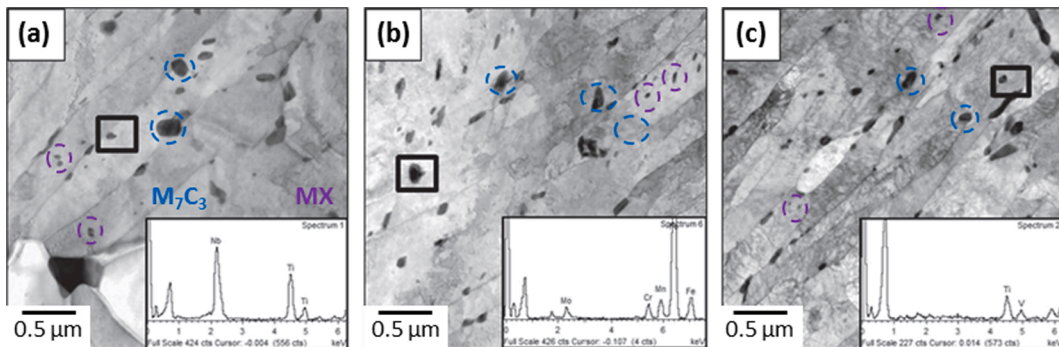


Fig. 2. TEM micrographs of X100Q quenched from (a) 875 °C, (b) 925 °C and (c) 975 °C, highlighting the presence of precipitates in the bainitic lath microstructure [30].

$$\lambda_k = 1.2\sqrt{\frac{3}{2}} \frac{r_k}{\sqrt{f_{k,eq}}} \quad (14)$$

where r_k is particle radius, $f_{k,eq}$ is the equivalent precipitate volume fraction and $k = c, m$ which denote M_7C_3 carbides and MX carbonitrides, respectively. It is assumed that MX carbonitrides are distributed uniformly throughout the microstructure; therefore, the equivalent volume fraction of MX carbonitrides is the measured volume fraction of particles, i.e. $f_{m,eq} = f_m$. However, M_7C_3 carbides are assumed to be dispersed along boundaries only, so that the equivalent volume fraction is:

$$f_{c,eq} = \frac{f_c}{f_g + f_w} \quad (15)$$

2.3. Yield strength

Yield strength is dependent on both the dislocation density and the presence of obstacles to slip within the microstructure [36]. For bainitic steels such as X100Q, the primary obstacles to slip include HABs, LABs, Peierls-Nabarro stress, and precipitates [37]. Therefore, these factors are incorporated in the physically-based isotropic yield strength implemented in this work, which is based on the work of Barrett and co-workers [19], where the cyclic yield strength is given by:

$$\sigma_y^{cyc} = k_y M \sqrt{\tau_A^2 + \tau_B^2} \quad (16)$$

where the constant k_y accounts for the thermal component of yield strength under cyclic deformation. The Taylor hardening expression is used to quantify the contribution of dislocation density to yield strength as follows:

$$\tau_A = \alpha_1 \mu b \sqrt{\rho} \quad (17)$$

where α_1 is the Taylor hardening coefficient (taken as 0.15 [38]) and ρ is dislocation density. The contribution of obstacles to the yield strength is assumed to be the sum of the individual obstacle strengthening contributions:

$$\tau_B = \tau_{HP} + \tau_{LAB} + \tau_{PN} + \tau_{ph} \quad (18)$$

where τ_{HP} is the contribution of HABs to strength, τ_{LAB} is the contribution of LABs to strength, τ_{PN} is the Peierls-Nabarro stress and τ_{ph} is the strengthening due to precipitates. The contribution of HABs to strength is modelled using a Hall-Petch relationship:

$$\tau_{HP} = \frac{k_{HP}}{d_g^{n_{HP}}} \quad (19)$$

where k_{HP} is the Hall-Petch constant and n_{HP} is the Hall-Petch exponent. The contribution of LABs to strength is inversely proportional to the effective lath width, \bar{m} , [39] and given by:

$$\tau_{LAB} = \frac{\alpha_2 \mu b}{\bar{m}} \quad (20)$$

where α_2 is a material constant (taken as 2.5 [19]). The Naylor mean slip length model [40] is used to determine the effective lath width:

$$\bar{m} = \frac{2}{\pi} \left[w \ln \left(\tan \left(\arccos \left(\frac{w}{l} \right) \right) + \frac{l}{w} \right) + l \frac{\pi}{2} - l \arccos \left(\frac{w}{l} \right) \right] \quad (21)$$

where l is the maximum bainitic lath dimension, which is assumed to be equal to the bainitic block width. The Peierls-Nabarro stress is determined as follows [41]:

$$\tau_{PN} = \frac{2\mu}{1-\nu} \exp \left(\frac{-2\pi}{1-\nu} \right) \quad (22)$$

The Ashby-Orowan equation [42] is used to determine the strengthening effect of precipitates due to dislocation pinning:

$$\tau_{ph,k} = 0.045 \frac{\mu b}{\lambda_k} \ln \frac{r_k}{b} \quad (23)$$

Following the logic of Eq. (8), a rule of mixtures approach is used to define the contribution of precipitates to the yield strength:

$$\tau_{ph} = (f_w + f_g) \tau_{ph,BND} + (1 - f_w - f_g) \tau_{ph,INT} \quad (24)$$

where $\tau_{ph,BND} = \tau_{ph,c} + \tau_{ph,m}$ and $\tau_{ph,INT} = \tau_{ph,m}$.

2.4. Dislocation density evolution

The overall dislocation density, ρ , within the microstructure is given by the sum of the mobile dislocation density, $\vec{\rho}$, and the volume-weighted immobile dislocation densities at HABs, LABs and in lath interiors, ρ_g , ρ_w and ρ_l respectively:

$$\rho = \vec{\rho} + f_w \rho_w + f_g \rho_g + (1 - f_w - f_g) \rho_l \quad (25)$$

The overall dislocation density varies as a function of accumulated effective inelastic strain due to growth, annihilation and immobilisation processes (i.e. $\dot{\rho} = \dot{\rho}^+ - \dot{\rho}^-$ [32]). In this work, the nucleation of both edge and screw dislocations is assumed to occur due to a Frank-Read source [43]. Reduction of dislocation density is assumed to occur due to mutual annihilation, LAB dislocation annihilation and the formation of dislocation dipoles and locks. The dislocation density evolution model implemented here is described in detail by Barrett et al. [17].

2.5. Bainitic lath width evolution

The bainitic lath substructure plays an essential role in attaining the strength and toughness [44] required for X100Q grade steel. The contribution of the laths to the constitutive behaviour is modelled here as a function of lath width, lath shape, and the angle of misorientation between adjacent laths. The coarsening of laths and formation of dislocation cell substructures occurs during cyclic inelastic loading due to annihilation of the lath boundaries. The resulting loss of both dislocations and obstacles to further dislocation movement contributes to the cyclic softening phenomenon [45] exhibited by X100Q [4]. The concomitant coarsening of laths with the reduction of LAB dislocation density ([46,47]) is given by [48]:

$$w = \frac{w_0 \rho_{w,0}}{\rho_w} \quad (26)$$

where w_0 and $\rho_{w,0}$ are the initial lath width and LAB dislocation density, respectively. Lath coarsening may occur until the maximum lath width, assumed here to equal the bainitic block size, d_g , is reached. The lath width evolution model is predicated on the idealised lath geometry shown in Fig. 3. Using this cuboid geometry, the lath perimeter is $4w(X_1 + X_2 + X_3)$ and the boundary surface area is $4s_0 \left(w(X_1 + X_2 + X_3) - \frac{s_0}{2} \right)$, such that the density of LAB dislocations is:

$$\rho_w = \frac{1}{2s} \frac{w(X_1 + X_2 + X_3)}{s_0 \left(w(X_1 + X_2 + X_3) - \frac{s_0}{2} \right)} \quad (27)$$

where s is the LAB dislocation spacing (defined based on the angle of misorientation, θ , as b/θ), and s_0 is the initial LAB dislocation spacing. The rate of change in misorientation between adjacent laths is defined as [17]:

$$\dot{\theta} = \frac{2b^2}{\theta_0} \dot{\rho}_w - \frac{b^3}{\theta_0^2 (X_1 + X_2 + X_3)} \left[\frac{w \dot{\rho}_w - \rho_w \dot{w}}{w^2} \right] \quad (28)$$

where θ_0 is the initial angle of lath misorientation. The volume fraction of LABs is also defined based on the idealised bainitic lath geometry

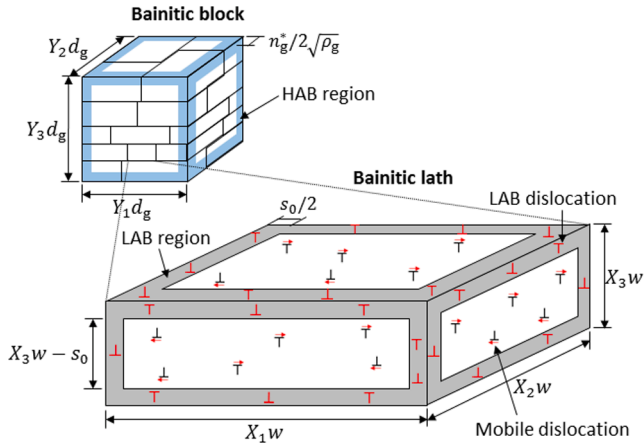


Fig. 3. The idealised bainitic block and lath geometries which are assumed for the determination of HAB and LAB volume fractions.

shown in Fig. 3, such that the volume fraction of LABs is:

$$f_w = \frac{V_w}{X_1 X_2 X_3 w^3} \quad (29)$$

where V_w is the bainitic lath volume, which is determined using the following equation:

$$V_w = X_1 X_2 X_3 w^3 - (X_1 w - s_0)(X_2 w - s_0)(X_3 w - s_0) \quad (30)$$

where the values of the lath characteristic length coefficients, X_1 , X_2 and X_3 are estimated as 5, 2 and 1 respectively based on TEM observations by Wang et al. [30] for X100Q.

2.6. Bainitic block model

Following the logic applied for the bainitic lath structure and based on the idealised bainitic block shown in Fig. 3, the HAB volume fraction is given by [17]:

$$f_g = 1 - \frac{(Y_1 d_g - n_g^* / \sqrt{\rho_g})(Y_2 d_g - n_g^* / \sqrt{\rho_g})(Y_3 d_g - n_g^* / \sqrt{\rho_g})}{Y_1 Y_2 Y_3 d_g^3} \quad (31)$$

where the block characteristic length coefficients, Y_i , are assumed as 1 and the HAB width is assumed as the product of n_g^* and the mean spacing of HAB dislocations, which is given by $s_g = 1 / \sqrt{\rho_g}$.

2.7. Fatigue damage

The cyclic softening behaviour exhibited by X100Q PM and simulated HAZ is a result of both the microstructural degradation mechanisms outlined here and fatigue damage accumulation [49]. In fact, the PM and simulated HAZ microstructures exhibit two-stage damage accumulation behaviour [4]. The softening effect of fatigue damage accumulation may be demarcated by considering the evolution of elastic modulus as follows [50]:

$$\hat{E} = E_0(1 - D) \quad (32)$$

where \hat{E} is the cyclic unloading modulus, E_0 is the initial modulus and D is fatigue damage. The two-stage damage accumulation comprises of early-life fatigue damage and secondary fatigue damage. Early-life fatigue damage is related to the formation of microcracks, and accumulates rapidly in the initial fatigue cycles before reaching a stabilised value which is maintained for the majority of life. On the other hand, secondary fatigue damage is associated with rapid crack propagation, and ultimately leads to failure. Further detail on the two-stage damage

model is given in previous work by the authors [49]. As the focus of this work is implementation of the physically-based constitutive model to predict the cyclic deformation behaviour of X100Q PM and simulated HAZ, the influence of early-life (primary) fatigue damage on the constitutive response is included for each material through degradation of the elastic modulus. Secondary fatigue damage, which relates to life prediction, is not included in this work. The early-life fatigue damage evolution is modelled as a function of accumulated effective plastic strain energy [49]:

$$D = \frac{\ln(Ep^2)}{K_1 \sigma_{\max,0}^{m_1}} \quad (33)$$

where p is the accumulated effective plastic strain and K_1 and m_1 are constants fitted to the experimentally observed accumulated effective plastic strain and damage evolutions using the least squares method. The early-life fatigue damage parameters identified for physically-based constitutive modelling of X100Q PM and simulated HAZ, via the identification process described in [49], are shown in Table 2.

2.8. Physically-based parameter identification

The X100Q PM and simulated FGHAZ block size are estimated from electronic backscatter diffraction scans, as shown in Fig. 4 [4], assuming a linear relationship between grain size and block size [51], and the ICHAZ block and lath size and FGHAZ lath size are estimated from optical microscopy images of an X100Q girth weld presented in [4]. The lath width for X100Q PM is estimated from the TEM micrograph shown in Fig. 2(b) [30]. The bainitic block and lath dimensions used for modelling are shown in Table 3.

The initial overall dislocation density for X100Q PM is estimated based on measurements reported by He et al. [44] for bainitic steels with a similar lath width. The values of mobile, HAB and lath interior immobile dislocation density are fitted using Eq. (25), by maintaining the proportions of mobile and immobile dislocation density reported by Barrett and co-workers [17]. The initial values of dislocation density used in this work are shown in Table 4. The initial values are assumed to be equal for X100Q PM and simulated HAZ in this work, as the LABs are the predominant source of dislocation density for this material.

The values of physically-based parameters used in the constitutive modelling framework are shown in Table 5. The temperature-independent Helmholtz free energy, ΔF , and pre-exponential viscous constant, A , parameters were identified from high-temperature stress relaxation test data for P91 steel, as described by Barrett et al. [17]. The constant, k_y , is fitted to room temperature low-cycle fatigue first- and half-life cycle response for X100Q PM. The Hall-Petch parameters, k_{HP} and n_{HP} , are fitted to experimental data for pure Fe ([52,53]). The value of initial lath misorientation angle presented by Barrett et al. [17] is used, which is within the range of 2-7° reported for bainitic laths ([44,54]).

3. Results

The predicted constitutive and fatigue responses of X100Q PM and simulated HAZ are compared against the experimentally obtained responses in the following section. Further details on the experimental methodology and results are presented by the authors elsewhere [4].

Table 2

The identified early-life fatigue damage parameters for X100Q PM and simulated HAZ.

Material	K_1 (-)	m_1 (-)
PM	1.3×10^5	-1
5 °C/s ICHAZ	2×10^5	-1
10 °C/s FGHAZ	3×10^5	-1

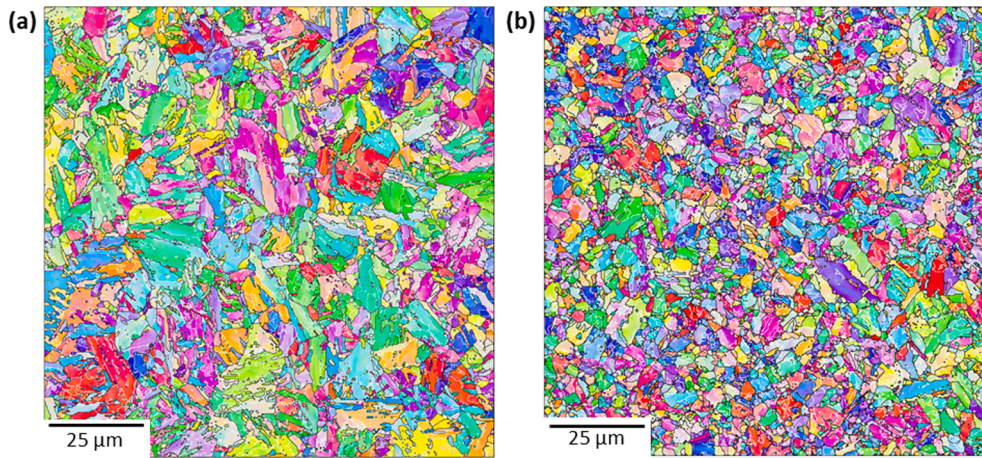


Fig. 4. Crystal orientation maps of (a) X100Q PM and (b) 10 °C/s simulated FGHAZ with LABs highlighted in white and HABs highlighted in black.

Table 3
The microstructural dimensions used for modelling of X100Q PM and simulated HAZ.

Material	Block size (μm)	Initial lath width (μm)
PM	5.1	0.34
5 °C/s ICHAZ	9	5
10 °C/s FGHAZ	3	1

Table 4
The initial mobile, HAB immobile and lath interior immobile dislocation densities used for modelling of X100Q PM and simulated HAZ.

Parameter	Value	Source
$\vec{\rho}_0$	$6.31 \times 10^{13} \text{ m}^{-2}$	Present work
ρ_s	$3.94 \times 10^{14} \text{ m}^{-2}$	Present work
ρ_i	$3.94 \times 10^{10} \text{ m}^{-2}$	Present work

Table 5
The values of physically-based material parameters used in the modelling framework.

Parameter	Value	Source
A	$1 \times 10^{16} \text{ s}^{-1}$	[17]
ΔF	$5.95 \times 10^{-19} \text{ J}$	[17]
k_B	$1.38 \times 10^{-23} \text{ m}^2 \text{ kg s}^{-2} \text{ K}^{-1}$	Physical constant
k_y	0.68	Present work
k_{HP}	$4.7 \text{ MPa mm}^{-1/2}$	[52,53]
n_{HP}	0.5	[52,53]
θ_0	2.86°	[17]

Comparisons of the predicted and measured stress–strain responses for X100Q PM, simulated ICHAZ and simulated FGHAZ at the first and half-life cycles, for 1.2%, 1% and 0.8% strain range fatigue tests are shown in Figs. 5 to 7. The model accurately captures the influence of microstructure, via differences in bainitic block size and lath width, and the effect of strain range on the initial and stabilised stress–strain responses for the three materials.

The simulated ICHAZ exhibits the softest response due to an increase in bainitic block size and a significant reduction in the prevalence of bainitic lath microstructure compared to the PM. The predicted response for the simulated ICHAZ is in close agreement with the experimental data for the first half-cycle of at each strain range; but the agreement diminishes thereafter due to compressive mean stress in the order of 50 MPa, which is present in the first cycle experimental data. However, the

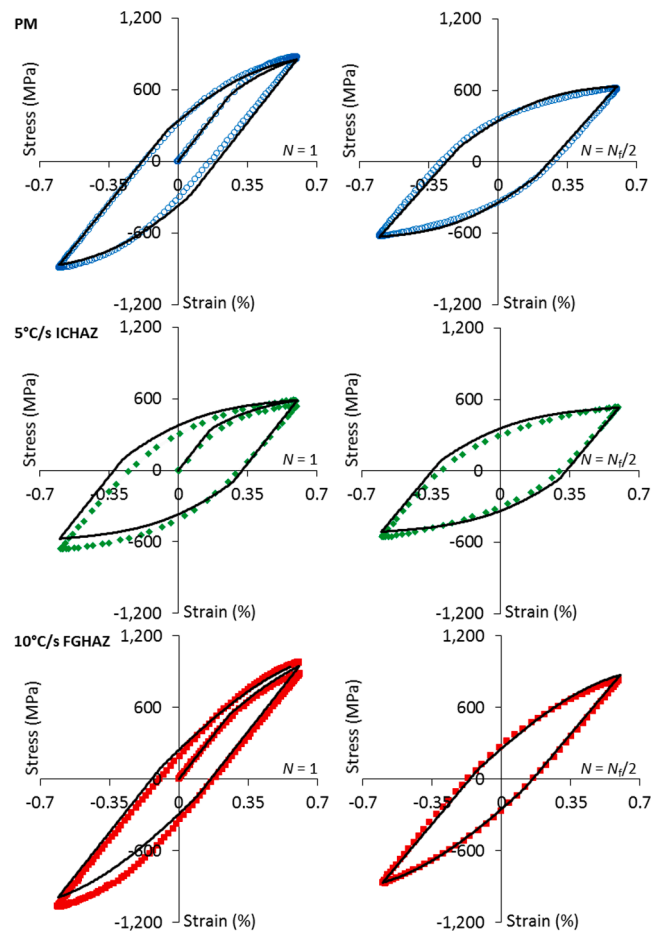


Fig. 5. The predicted and measured stress–strain response for X100Q PM and simulated HAZ at the first and half-life cycles for a 1.2% strain range test.

compressive mean stress is essentially absent at the half-life cycles, where close agreement is recovered between the predicted and measured responses.

The strongest initial and stabilised response is exhibited by the simulated FGHAZ, which is attributed to a reduction in bainitic block size and the prevalence of bainitic lath microstructure compared to the PM. A similar trend to simulated ICHAZ is shown in the comparison between the predicted and experimental first cycle response for simulated FGHAZ, with good agreement being shown for the first half-cycle.

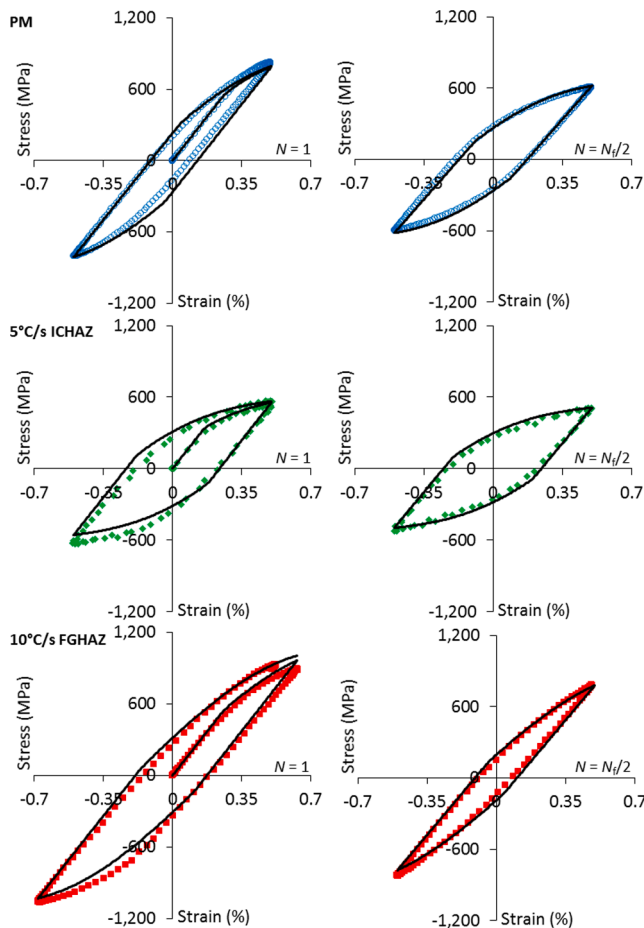


Fig. 6. The predicted and measured stress–strain response for X100Q PM and simulated HAZ at the first and half-life cycles for a 1% strain range test.

The agreement between predicted and measured half-life response is very close for the 1.2% and 1% strain range tests, but the quality of the fit is reduced for the 0.8% strain range, again due to the compressive mean stress of approximately 60 MPa in the experimental data.

The capability of the damage-coupled physically-based constitutive model to capture the evolution in stress amplitude as a result of microstructural degradation and early-life fatigue damage is shown by the comparison between the predicted and measured stress amplitude and damage evolutions of X100Q PM, simulated ICHAZ and simulated FGHAZ for 1.2%, 1% and 0.8% strain range fatigue tests, shown in Figs. 8 to 10. The final failure behaviour is not captured by the model as secondary fatigue damage is not considered in this work.

A comparison of the predicted overall dislocation density evolutions during the first 2,000 cycles for a% strain range fatigue test is shown in Fig. 11. The predicted evolutions are qualitatively in agreement with experimental results presented by Zhou et al. [55] for fatigue of a low-carbon bainitic steel. The overall dislocation density is highest in X100Q PM, which is primarily due to its fine bainitic lath structure. This high dislocation density initially rises but then decreases significantly with cyclic deformation, as a result of LAB dislocation annihilation and lath coarsening. The predicted dislocation densities of simulated ICHAZ and simulated FGHAZ are lower due to their coarser initial bainitic lath structures. Their dislocation densities fall sharply during the initial cycles before reaching an essentially stable value. The calculated initial dislocation density for simulated FGHAZ is within the range of 4.4 to $4.7 \times 10^{14} \text{ m}^{-2}$ reported by Wang and co-workers [30] for X100Q quenched from peak temperatures between $875 \text{ }^\circ\text{C}$ and $975 \text{ }^\circ\text{C}$.

The predicted LAB and mobile dislocation density evolutions during the first 2,000 cycles for a 1% strain range fatigue test are shown in

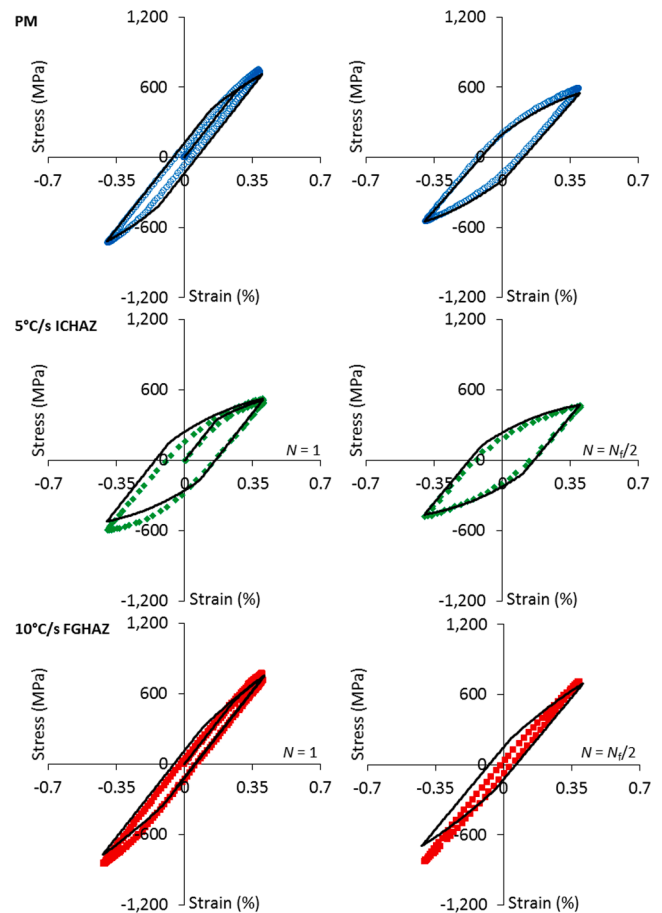


Fig. 7. The predicted and measured stress–strain response for X100Q PM and simulated HAZ at the first and half-life cycles for a 0.8% strain range test.

Fig. 12. Although the initial LAB dislocation density is similar for the PM and simulated HAZ materials, the rate of decrease in LAB dislocation density is greatest in the PM due to its fine bainitic lath microstructure. The same initial mobile dislocation density is assumed for each material; however, the density in the PM rises rapidly over the first 20 cycles, whereas the density in the simulated ICHAZ and simulated FGHAZ falls sharply over the first 10 cycles. This contrast in the evolution of mobile dislocation density is reflected in the predicted overall dislocation density evolutions.

The predicted lath width evolutions during the first 2,000 cycles for a 1% strain range fatigue test are shown in Fig. 13. In correlation with the trends predicted for LAB dislocation density, X100Q PM lath width is predicted to increase by almost 175%, while the simulated ICHAZ and FGHAZ lath widths are predicted to increase by 35% and 60% respectively.

In Fig. 14, the predicted evolutions of overall dislocation density with lath width for X100Q PM, simulated ICHAZ and simulated FGHAZ are compared against experimental measurements of dislocation density and lath width from bainitic and ferritic steels [13]. The predicted correlation between dislocation density and lath width for PM follows the trend shown in the experimental data and the predicted correlations for simulated ICHAZ and simulated FGHAZ are within the range of the experimentally measured values.

The predicted evolutions of cyclic yield strength during the first 2,000 cycles for a 1% strain range fatigue test are shown in Fig. 15. The initial yield strengths follow the trends shown during tensile characterisation [4], with the predicted yield strength for X100Q PM being slightly higher than for simulated FGHAZ due to the influence of bainitic lath microstructure, and the predicted value for simulated ICHAZ being

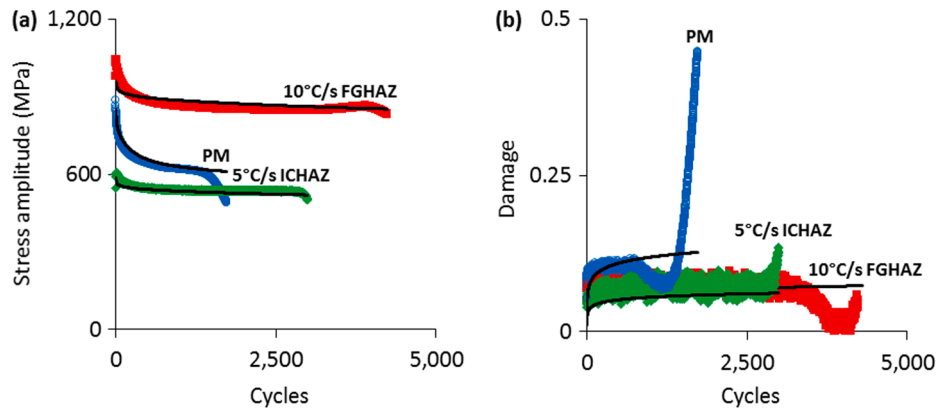


Fig. 8. The predicted and measured (a) stress amplitude evolution and (b) damage accumulation for X100Q PM and simulated HAZ for a 1.2% strain range test.

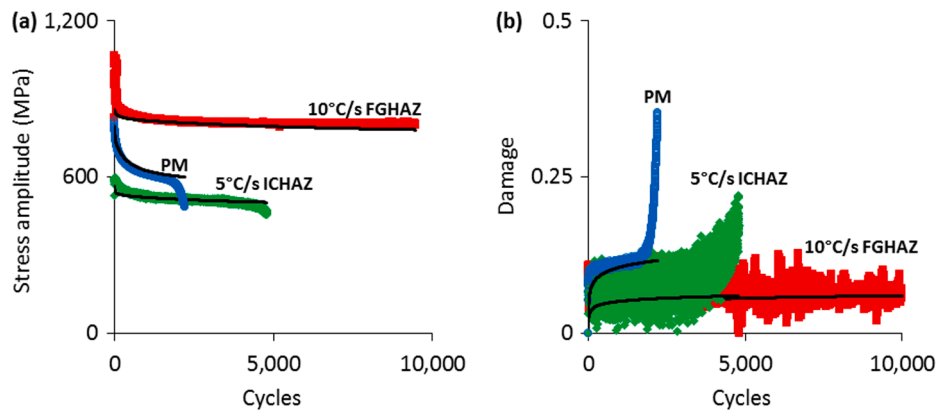


Fig. 9. The predicted and measured (a) stress amplitude evolution and (b) damage accumulation for X100Q PM and simulated HAZ for a 1% strain range test.

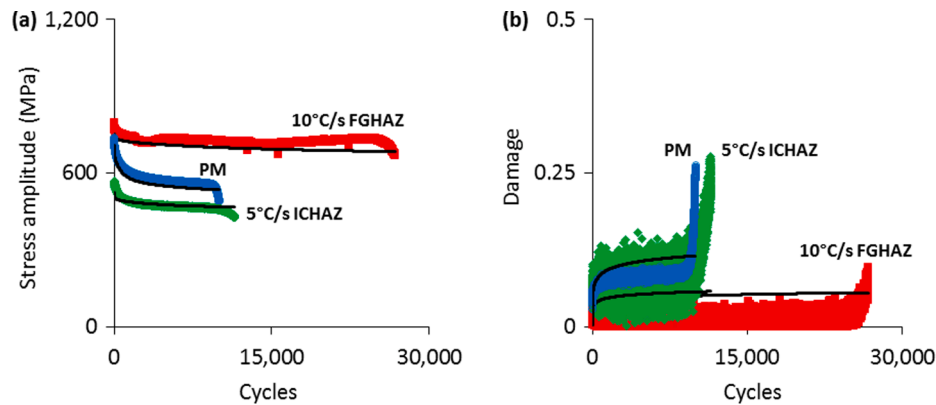


Fig. 10. The predicted and measured (a) stress amplitude evolution and (b) damage accumulation for X100Q PM and simulated HAZ for a 0.8% strain range test.

significantly lower. However, the yield strength in X100Q PM is predicted to cyclically soften rapidly in comparison to the values for simulated HAZ, due to the influence of dislocation annihilation and lath coarsening, as shown in Fig. 11 and Fig. 13, respectively.

The contributions of dislocations and obstacles to the predicted shear strength at the first cycle and near the failure cycle for X100Q PM and simulated HAZ for a 1% strain range test are shown in Fig. 16. At the first cycle, dislocations and HABs are predicted to be the primary contributors to strength for each material. The contribution of LAB strengthening varies significantly with lath width. LABs contribute significantly to strength for X100Q PM and simulated FGHAZ but provide a relatively low contribution to strength for simulated ICHAZ, where the effective lath width is significantly higher. The predicted contributions of

precipitates to strength for X100Q PM and simulated HAZ materials are all within 30% of the value reported by Niu and co-workers for X100 PM [56].

Near the failure cycle, the predicted strengthening contributions of dislocations and LABs are significantly reduced, primarily due to LAB dislocation annihilation and lath coarsening. The resultant softening is greatest for X100Q PM, whereas simulated ICHAZ and FGHAZ soften to a lesser extent due to the lower contributions of dislocation and LAB strengthening to their initial strength.

A comparison of the cyclic softening predicted for X100Q PM and simulated HAZ, with and without the effect of early-stage fatigue damage, for a 1% strain range test is shown in Fig. 17. Fatigue damage is the major contributor to the predicted cyclic softening for each material,

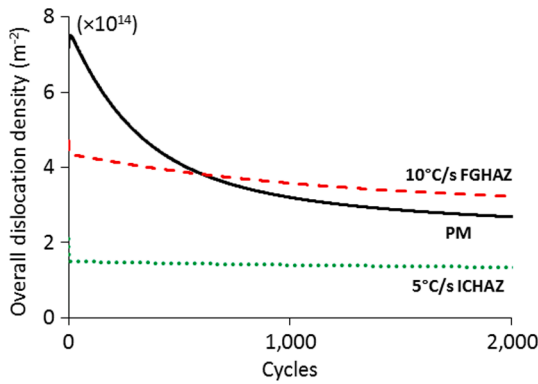


Fig. 11. The predicted evolution of overall dislocation density for X100Q PM and simulated HAZ for a 1% strain range test.

with microstructural degradation, as a result of LAB dislocation annihilation and lath coarsening also contributing significantly to the predicted softening for PM.

4. Discussion

A key novelty of this work is the incorporation of dislocation annihilation, lath coarsening and early-life fatigue damage mechanisms to capture the cyclic softening behaviour exhibited by X100Q PM and simulated HAZ. The damage-coupled physically-based constitutive model implemented here successfully predicts the influence of microstructure on constitutive response for PM, simulated ICHAZ and simulated FGHAZ, via bainitic block and lath dimensions.

The proposed dislocation mechanics model, based on a rule of mixtures formulation, combining mobile and immobile dislocation densities, including HAB, LAB and lath interior contributions, based on measured and inferred microstructure data, is shown to agree with experimental data. Specifically, for example, the model-computed initial dislocation density for simulated FGHAZ agrees closely to measured values [30]. Similarly, the model captures the measured microstructural effects of lath width on dislocation density between the different welding-affected zones for PM and simulated HAZ [13]. The resulting model representation of heterogeneous dislocation strengthening due to welding is also in agreement with the experimental observations of He and co-workers [44] vis-à-vis refinement or coarsening of lath width for bainitic and ferritic steels.

The fine bainitic lath microstructure and high dislocation density of X100Q PM are predicted to contribute significantly to the high initial strength of the material; however, significant softening is predicted to occur under cyclic deformation due to LAB dislocation annihilation and

lath coarsening. The substantial strengthening contribution of bainitic block size for simulated FGHAZ, which is refined due to rapid austenisation and recrystallization during welding, is maintained under cyclic deformation; as a result, simulated FGHAZ is predicted to have the highest cyclic strength. The bainitic block and lath microstructure in simulated ICHAZ are coarsened significantly due to partial transformation during the welding process. Although the extent of cyclic softening due to dislocation annihilation and lath coarsening is low for this material, both the initial and cyclic strength of simulated ICHAZ are predicted to be less than for PM or simulated FGHAZ, due to the coarsened bainitic block microstructure.

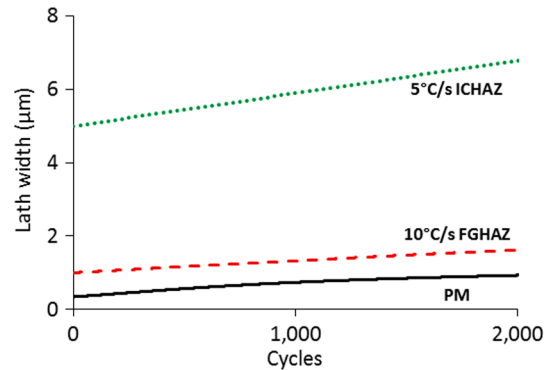


Fig. 13. The predicted lath width evolution for X100Q PM and simulated HAZ for a 1% strain range test.

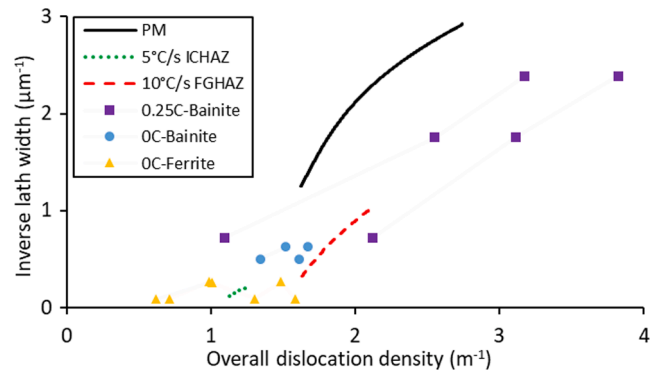


Fig. 14. Comparison between the predicted evolutions of overall dislocation density with lath width for X100Q PM and simulated HAZ against experimental measurements from bainitic and ferritic steels pre- and post-tensile deformation [13].

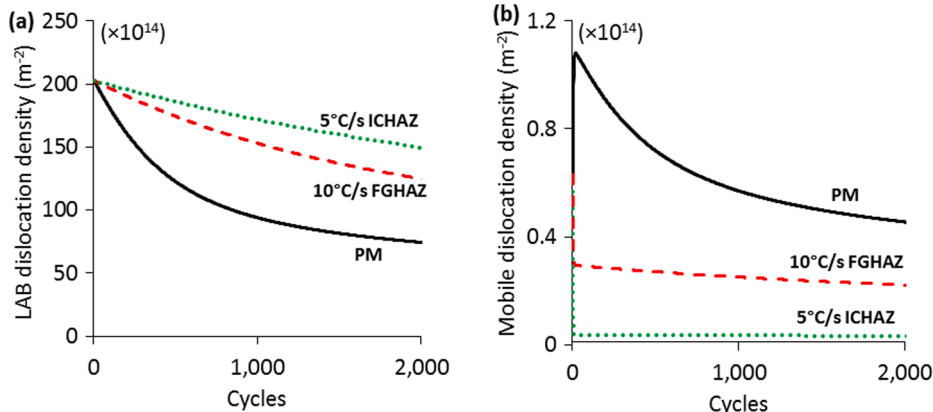


Fig. 12. The predicted evolutions of (a) LAB and (b) mobile dislocation density for X100Q PM and simulated HAZ during for a 1% strain range test.

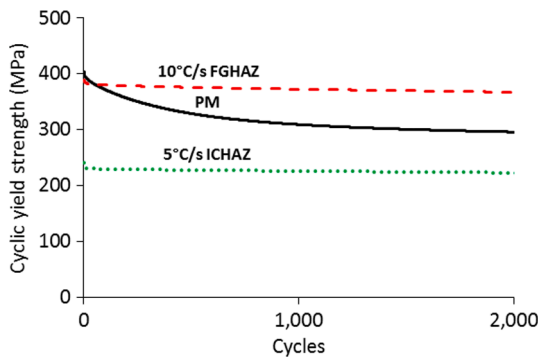


Fig. 15. The predicted evolution of cyclic yield strength for X100Q PM and simulated HAZ for a 1% strain range test.

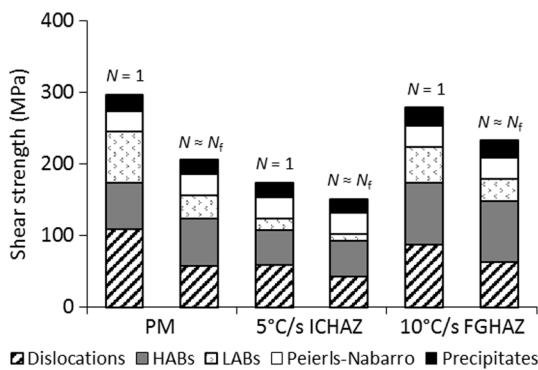


Fig. 16. The predicted contributions to shear strength at the first cycle and near the failure cycle for X100Q PM and simulated HAZ for a 1% strain range test.

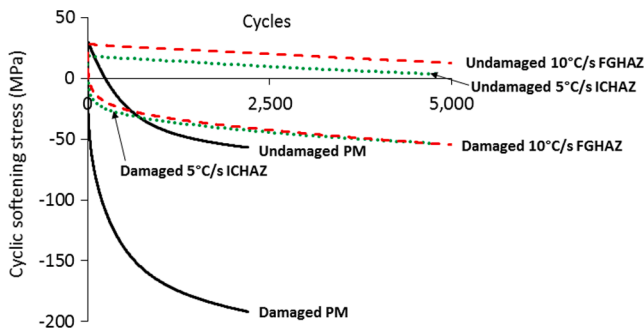


Fig. 17. Comparison between the predicted cyclic softening for X100Q PM and simulated HAZ, with and without the effect of early-life fatigue damage, for a 1% strain range test.

This work demonstrates a capability to predict the differences in cyclic plasticity and fatigue damage response for the PM and sampled weld-affected microstructural regions (ICHAZ, FGHAZ). In future work, it is proposed that the methodology be used to predict the full spatial distribution of inhomogeneous constitutive and fatigue damage responses, across welded joints. This could be achieved by coupling the present model to a through-process microstructural evolution model, such as that described by Mac Ardghail and co-workers [57].

The close agreement shown between the model predicted and experimental constitutive responses indicates the potential for implementation of the model with a plastic strain or energy-based fatigue life prediction methodology, such as that developed by Golos [58].

5. Conclusions

A physically-based constitutive model for the fatigue of X100Q welds, including the influence of dislocations, HABs, LABs, precipitates and crystal lattice stress on yield strength and nonlinear strain hardening response, has been implemented. The constitutive model has been coupled with an early-life fatigue damage model [49] to predict the cyclic plastic response of three X100Q weld regions; PM, simulated ICHAZ and simulated FGHAZ. The key conclusions from this work are:

- The damage-coupled physically-based constitutive model successfully captures the differences in bulk cyclic deformation behaviour between X100Q PM, simulated ICHAZ and simulated FGHAZ via direct representation of bainitic block and lath dimensions for the three weld regions. This represents a key step in predicting the inhomogeneous constitutive and fatigue damage performance of X100Q welded connections.
- The predicted dislocation density evolutions follow the trends shown in the literature for bainitic steels and the predicted relationship between lath width and dislocation density is in general agreement with experimental data for bainitic and ferritic steels.
- Refinement in block size is predicted to be beneficial for both monotonic and cyclic strength, whereas the strengthening effect of a fine bainitic lath microstructure reduces with cyclic deformation due to LAB dislocation annihilation and lath coarsening, resulting in cyclic softening.
- The model successfully predicts the experimentally observed bulk cyclic softening and early-life fatigue damage accumulation behaviour of X100Q PM, simulated ICHAZ and simulated FGHAZ. Fatigue damage is predicted to be the major contributor to cyclic softening for each material.

Declaration of Competing Interest

The authors declare that they have no known competing financial interests or personal relationships that could have appeared to influence the work reported in this paper.

Acknowledgements

This publication has emanated from research conducted the financial support of Science Foundation Ireland as part of the MECHANICS joint project between NUI Galway and University of Limerick under grant number SFI/14/IA/2604 and the I-Form Advanced Manufacturing Research Centre under grant number SFI/16/RC/3872.

Data availability statement

The raw/processed data required to reproduce these findings cannot be shared at this time as the data also forms part of an ongoing study.

References

- [1] Cunningham R. *The Stones Development: A New Vision in the ultra-deepwater Gulf of Mexico*. Houston: PennWell Custom Publishing; 2017.
- [2] Devaney RJ, O'Donoghue PE, Leen SB. Global and local fatigue analysis of X100 and X60 steel catenary riser girth welds. *J Struct Integr Maint* 2017;2(3):181–9.
- [3] Mecozzi E, et al. EUR 24214 - Fatigue behaviour of high-strength steel-welded joints in offshore and marine systems (FATHOMS). Luxembourg 2010.
- [4] Devaney RJ, O'Donoghue PE, Leen SB. Effect of Welding on Microstructure and Mechanical Response of X100Q Bainitic Steel through Nanoindentation, Tensile, Cyclic Plasticity and Fatigue Characterisation. *Mater Sci Eng A*. Under Review.
- [5] Easterling K. *Introduction to the Physical Metallurgy of Welding*. 2nd ed. Oxford: Butterworth-Heinemann; 1992.
- [6] Farragher TP, Scully S, O'Dowd NP, Hyde CJ, Leen SB. High Temperature, Low Cycle Fatigue Characterization of P91 Weld and Heat Affected Zone Material. *J Press Vessel Technol* 2014;136(2):1–10.
- [7] Touboul M, Crepin J, Rousselier G, Latourte F, Leclercq S. Identification of Local Viscoplastic Properties in P91 Welds from Full Field Measurements at Room Temperature and 625 °C. *Exp Mech* 2013;53(3):455–68.

- [8] Volterra V. Sur l'équilibre des corps élastiques multiplément connexes. *Ann Sci l'École Norm Supérieure* 1907;24:401–517.
- [9] Bergström Y. A dislocation model for the stress-strain behaviour of polycrystalline α -Fe with special emphasis on the variation of the densities of mobile and immobile dislocations. *Mater Sci Eng* 1970;5(4):193–200.
- [10] Roberts W, Bergström Y. The stress-strain behaviour of single crystals and polycrystals of face-centered cubic metals—a new dislocation treatment. *Acta Metall* 1973;21(4):457–69.
- [11] Mecking H, Kocks UF. Kinetics of flow and strain-hardening. *Acta Metall* 1981;29(11):1865–75.
- [12] Kocks UF, Mecking H. Physics and phenomenology of strain hardening: the FCC case. *Prog Mater Sci* 2003;48(3):171–273.
- [13] He SH, He BB, Zhu KY, Huang MX. Evolution of dislocation density in bainitic steel: Modeling and experiments. *Acta Mater* 2018;149:46–56.
- [14] Estrin Y, Tóth LS, Molinari A, Bréchet Y. A dislocation-based model for all hardening stages in large strain deformation. *Acta Mater* 1998;46(15):5509–22.
- [15] Roters F, Raabe D, Gottstein G. Work hardening in heterogeneous alloys—a microstructural approach based on three internal state variables. *Acta Mater* 2000;48(17):4181–9.
- [16] Magnusson H, Sandström R. Creep Strain Modeling of 9 to 12 Pct Cr Steels Based on Microstructure Evolution. *Metall Mater Trans A* 2007;38(9):2033–9.
- [17] Barrett RA, O'Donoghue PE, Leen SB. A physically-based constitutive model for high temperature microstructural degradation under cyclic deformation. *Int J Fatigue* 2017;100:388–406.
- [18] Hosseini E, Kazeminezhad M. A new microstructural model based on dislocation generation and consumption mechanisms through severe plastic deformation. *Comput Mater Sci* 2011;50(3):1123–35.
- [19] Barrett RA, O'Donoghue PE, Leen SB. A physically-based high temperature yield strength model for 9Cr steels. *Mater Sci Eng A* 2018;730:410–24.
- [20] Rosenberg JM, Piehler HR. Calculation of the taylor factor and lattice rotations for bcc metals deforming by pencil glide. *Metall Trans* 1971;2:257–9. <https://doi.org/10.1007/BF02662666>.
- [21] Dieter GE, Bacon D. *Mechanical Metallurgy*. 3rd ed. London: McGraw-Hill; 1989.
- [22] Zhang ZF, Wang ZG. Comparison of fatigue cracking possibility along large- and low-angle grain boundaries. *Mater Sci Eng A* 2000;284(1–2):285–91.
- [23] Ashby MF, Jones DRH. *Engineering Materials 1: An Introduction to Properties, Applications, and Design*. 4th ed. Oxford: Elsevier; 2012.
- [24] Edalati K, Horita Z. High-pressure torsion of pure metals: Influence of atomic bond parameters and stacking fault energy on grain size and correlation with hardness. *Acta Mater* 2011;59(17):6831–6.
- [25] Sinclair CW, Poole WJ, Bréchet Y. A model for the grain size dependent work hardening of copper. *Scr Mater* 2006;55(8):739–42.
- [26] Bardel D, Perez M, Nelias D, Dancette S, Chaudet P, Massardier V. Cyclic behaviour of a 6061 aluminium alloy: Coupling precipitation and elastoplastic modelling. *Acta Mater* 2015;83:256–68.
- [27] Keller C, Margulies MM, Hadjem-Hamouche Z, Guillot I. Influence of the temperature on the tensile behaviour of a modified 9Cr–1Mo T91 martensitic steel. *Mater Sci Eng A* 2010;527(24–25):6758–64.
- [28] Li JC. Some elastic properties of an edge dislocation wall. *Acta Metall* 1960;8(8):563–74.
- [29] Li JCM, Chou YT. The role of dislocations in the flow stress grain size relationships. *Metall Mater Trans B* 1970;1(5):1145.
- [30] Wang H. et al. Effect of quenching temperature on microstructure and yield strength of Q-T-treated X100Q bainitic steel. *Mater. Res. Express*, vol. 5, 2018.
- [31] Silva R, Pinto A, Kuznetsov A, Bott I. Precipitation and Grain Size Effects on the Tensile Strain-Hardening Exponents of an API X80 Steel Pipe after High-Frequency Hot-Induction Bending. *Metals (Basel)* 2018;8(3):168.
- [32] Hart E. Theory of dispersion hardening in metals. *Acta Metall* 1972;20(2):275–89.
- [33] Taylor GI. Plastic Strain in Metals. *J Inst Met* 1938;62:307–24.
- [34] Ijiri Y, Oono N, Ukai S, Ohtsuka S, Kaito T, Matsukawa Y. Oxide particle–dislocation interaction in 9Cr-ODS steel. *Nucl Mater Energy* 2016;9:378–82.
- [35] Kocks UF. On the spacing of dispersed obstacles. *Acta Metall* 1966;14(11):1629–31.
- [36] Kocks UF, Argon AS, Ashby MF. Thermodynamics and Kinetics of Slip. *Prog Mater Sci* 1975;19:156–249.
- [37] Yakubtsov IA, Poruks P, Boyd JD. Microstructure and mechanical properties of bainitic low carbon high strength plate steels. *Mater Sci Eng A* 2008;480(1–2):109–16.
- [38] Bandyopadhyay PS, Ghosh SK, Kundu S, Chatterjee S. Evolution of Microstructure and Mechanical Properties of Thermomechanically Processed Ultra high-Strength Steel. *Metall Mater Trans A* 2011;42(9):2742–52.
- [39] Maruyama K, Sawada K, Koike J. Strengthening Mechanisms of Creep Resistant Tempered Martensitic Steel. *ISIJ Int* 2001;41(6):641–53.
- [40] Naylor JP. The influence of the lath morphology on the yield stress and transition temperature of martensitic–bainitic steels. *Metall Trans A* 1979;10(7):861–73.
- [41] Nabarro FRN. Dislocations in a simple cubic lattice. *Proc Phys Soc* 1947;59(2):256–72.
- [42] Ashby MF. The theory of the critical shear stress and work hardening of dispersion-hardened crystals. In: *Proceedings of the Second Bolton Landing Conference on Oxide Dispersion Strengthening*; 1968. p. 143–205.
- [43] Frank FC, Read WT. Multiplication Processes for Slow Moving Dislocations. *Phys Rev* 1950;79(4):722–3.
- [44] He SH, He BB, Zhu KY, Huang MX. On the correlation among dislocation density, lath thickness and yield stress of bainite. *Acta Mater* 2017;135:382–9.
- [45] Mayer T, Balogh L, Solenthaler C, Müller Gubler E, Holdsworth SR. Dislocation density and sub-grain size evolution of 2CrMoNiWV during low cycle fatigue at elevated temperatures. *Acta Mater* 2012;60(6–7):2485–96.
- [46] Saizay M, et al. Cyclically induced softening due to low-angle boundary annihilation in a martensitic steel. *Mater Sci Eng A* 2005;400–401(1–2 SUPPL.):241–4.
- [47] Saizay M, Fournier B, Mottot M, Pineau A, Monnet I. Cyclic softening of martensitic steels at high temperature—Experiments and physically based modelling. *Mater Sci Eng A* 2008;vol. 483–484, no. 1–2 C:410–4.
- [48] Giroux P-F. Experimental study and simulation of cyclic softening of tempered martensite ferritic steels. PhD Thesis, École Nationale Supérieure des Mines de Paris 2011.
- [49] Devaney RJ, O'Donoghue PE, Leen SB. Experimental characterisation and computational modelling for cyclic elastic-plastic constitutive behaviour and fatigue damage of X100Q for steel catenary risers. *Int J Fatigue* 2018;116:366–78.
- [50] Lemaitre J, Dufailly J. Damage measurements. *Eng Fract Mech* 1987;28(5–6):643–61.
- [51] Bhadeshia HKDH. *Bainite in Steels: Theory and Practice*. 3rd ed. London: CRC Press; 2015.
- [52] Sakui S, Sakai T. The Effect of Strain Rate, Temperature and Grain Size on the Lower Yield Stress and Flow Stress of Polycrystalline Pure Iron. *Tetsu-to-Hagane* 1972;58(10):1438–55.
- [53] Sakui S, Sakai T. The Effect of Grain Size on High Temperature Plastic Deformation of Polycrystalline Pure Iron. *J Japan Inst Met* 1976;40(3):263–9.
- [54] Zhu K, Bouaziz O, Oberbillig C, Huang M. An approach to define the effective lath size controlling yield strength of bainite. *Mater Sci Eng A* 2010;527(24–25):6614–9.
- [55] Zhou Q, Qian L, Meng J, Zhao L, Zhang F. Low-cycle fatigue behavior and microstructural evolution in a low-carbon carbide-free bainitic steel. *Mater Des* 2015;85:487–96.
- [56] Niu T, Kang Y, Gu H, Yin Y, Qiao M. Precipitation Behavior and Its Strengthening Effect of X100 Pipeline Steel. *J Iron Steel Res Int* 2010;17(11):73–8.
- [57] Mac Ardghail P, Harrison N, Leen SB. A process-structure-property model for welding of 9Cr power plant components: The influence of welding process temperatures on in-service cyclic plasticity response. *Int J Press Vessel Pip* 2019;173:26–44.
- [58] Golos KM. A total strain energy density model of metal fatigue. *Strength Mater* 1995;27(1–2):32–41.